# Biophysical Characteristics of Cholera Toxin and *Escherichia coli* Heat-Labile Enterotoxin Structure and Chemistry Lead to Differential Toxicity

John W. Craft, Jr.,[†] Tsai-wei Shen,[†] Lindsey M. Brier,[‡] and James M. Briggs[*]

Department of Biology and Biochemistry, University of Houston, 4800 Calhoun Road, Houston, Texas 77204-5001, United States

S *Supporting Information*

ABSTRACT: The biophysical chemistry of macromolecular complexes confer their functional characteristics. We investigate the mechanisms that make the AB5 holotoxin of *Vibrio cholerae* (CT) a significantly more pathogenic molecule than the enterotoxin of *Escherichia coli* (LT) with which it shares 88% similarity and whose structure is homologous with a backbone RMSD of 0.84 Å and imposes its deleterious effects though the same process to constitutively ADP-ribosylate adenylate cyclase. We present computational data that characterizes the impact of amino acid variations in the A2 tail, which helps to explain experimental data that demonstrate CT's higher toxicity. A hydrophobic patch on the B pentamer interface and its interactions with the A subdomain are partially disrupted by the substitution of an aspartic acid (LT) for glycine in CT. CT's holotoxin has less solvent accessible surface area (94 Å^2 vs 54 Å^2) and higher contact area (280 Å^2 vs 241 Å^2) with S228, which

is a gatekeeper, partially controlling the diffusion of water into the pore. CT excludes water from the top of the central pore whereas LT allows much more water to interact. These biophysical properties of the toxins lead to their differential toxicity and resulting impact to human health.
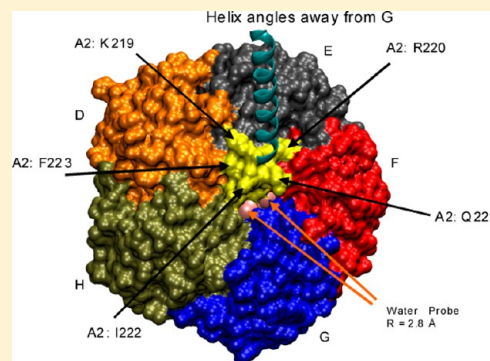
1. INTRODUCTION

The secreted AB$_5$ enterotoxins of *Vibrio cholerae*, cholera toxin (CT),[1−4] and *Escherichia coli*, heat-labile enterotoxin (LT),[5,6] share structural and functional homology. In fact, the structural topology is virtually identical where the A subunits of CT and LT share 82% sequence identity (88% similarity) and the B subunits share 80% sequence identity (87% similarity). Yet despite the very high level of identity between these two proteins, their differences in biophysical properties govern the consequences on organism pathology. Both are intracellular acting toxins[7,8] and members of the AB$_5$ family of bacterial toxins, which are composed of a 27 kDa A subunit and five 11 kDa B subunits[1] (Figure 1).

Cholera infects the cell through a retrograde transportation process that starts with the binding of ganglioside (GM1) on the membrane and association with lipid rafts.[9] The retrograde pathway interacts with the Golgi and reaches the endoplasmic reticulum (ER). A number of processing steps prepare the toxins for its catalytic function. These include the cleavage at a serine protease site R192, which divides the A subunit into an A1 and A2 peptide.[10] The A2 peptide includes the C-terminal residues from 193 to 240 of which residues 223−240 are in the central pore of the B pentamer. In addition, the reduction of a disulfide bond from residues 187−199 is required for CT to be active. A conserved KDEL endoplasmic reticulum protein retention receptor signal is present in CT.[11] The conserved signal in LT is RDEL and in both toxins the protein can be recycled back from the Golgi to the ER, likely increasing the number of
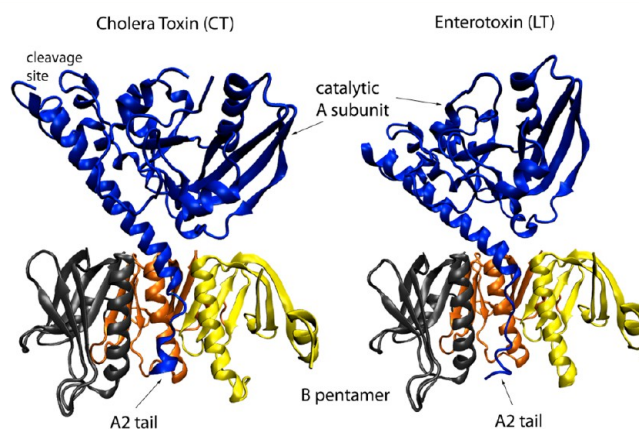

Figure 1. Cholera toxin (CT: 1S5E[4]) and heat-labile enterotoxin (LT: 1LTS[6]). The two toxins share a common topology. Notice the difference in the confirmations in the A2 tail. Rendered in VMD and colored by chain. The A subunit is in blue and includes the catalytic domain. The B pentamer includes the chains E, F, and G in yellow, rust, and black, respectively, and chains D and H were removed so that the central pore is visible.

---

toxin molecules that accumulate in the ER. In the ER the A subunit of the toxin has interactions with protein disulfide isomerase (PDI)[12,13] to unfold it for continuing the retrograde journey across the ER membrane into the cytosol, mediated by a number of proposed proteins like BiP[9] and Sec61β.[14] Both LT and CT are ADP-ribosylating bacterial toxins with a catalytic A1 subunit that refolds in the cytosol and activates adenylate cyclase by constitutively ADP-ribosylating G-proteins, with a common mechanism of action. Rodighiero et al.[15] demonstrated that the catalytic efficiency of the A1 subunits of CT and LT are similar as measured by an agmatine assay. Despite the shared characteristics between these toxins, the outcomes as measured in human health are significantly higher in CT. Though these differential outcomes may be influenced by numerous ecological, immunological, and systems effects, a set of remarkable experiments were completed by Rodighiero et al.,[15] in which they swapped sequence segments between the two toxins and assayed toxin-induced Cl⁻ ion secretion in polarized human epithelial (T84) cells. Those experiments point to differences in each toxin's macromolecule biophysical characteristics as contributing to Cholera's higher health impact. The region of the A2 C-terminus that was exchanged was the 16 residues from amino acids 225−240, which includes six amino acid differences G225D, D229E, I230V, T232I, H233Y, and K237R (Table 1).

Table 1. A2 Tail Sequences of CT and LT

Configuration	A2 Sequence (Y214 – L240)
CT: WT	YQSKVKRQIFSGYQSDIDTHNRIKDEL
LT: WT	***********D***EV*IY***R***

This spans the portion of the A2 tail that is within the B pentamer pore and is likely to influence the stability of the A subdomain interactions within the pore.[15] They found that a construct of CT that had an LT tail significantly attenuated Cl⁻ ion secretion by impacting both the time course (100 vs 175 min to maximum) and the maximum current (70 vs 48 μA/cm²) (Figure 2). On the other hand, a construct of LT
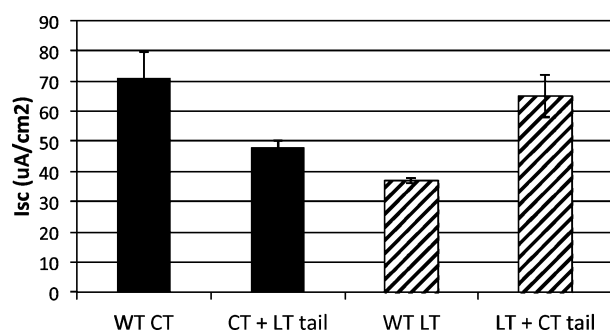

Figure 2. Differential toxicity between CT and LT. The figure is generated by summarizing data in Rodighiero et al.[15] Solid: reduced toxicity of CT with a LT tail. Hash: increased toxicity of LT with a CT tail.

that had a CT tail enhanced the response (160 vs 140 min to maximum) and (35 vs 65 μA/cm²).

Rodighiero et al.[15] also assayed a single point mutation K237R and found it was not responsible for the differential toxicity as expected because both a KDEL or an RDEL sequence are recognized by the endoplasmic reticulum protein

retention receptor. Ampapathi et al. hypothesize that this elongation, and therefore exposure of the KDEL termination sequence, could be an important aspect of the toxin's ability to undergo retrograde transport of the complex to the ER.[16] Assembly of CT wild-type, CTA-F223D, and CTA-F223H/CTB-T78D mutants were characterized by Tinker et al.[17] They also performed individual site-directed mutagenesis of I74, L77, and T78 in the B pentamer and found that each mutant disrupted assembly.[17] Interestingly, they found the CTA-F223D mutant to have lower assembly success and that the CTA-F223H/CTB-T78D double mutant rescued assembly outcomes. Though a F223D mutant might test the importance of a hydrophobic interaction between the A subunit and the B pentamer, it is actually a conserved residue between CT and LT. The two organisms, however, display a sequence deviation at residue 225, where in CT it is a glycine and in LT it is an aspartic acid (Table 1).

The crystal structure of CT by Zhang et al.[2] has helical propensity in the C-terminal tail (1XTC) and the crystal structures of CT by O'Neal et al.[4] revealed that the C-terminus of A2 in CT had more extended coil characteristics (1S5E). The crystal structure of LT by Sixma et al.[6] displayed more random coil content (1LTS). Computational techniques were used to evaluate changes in nonbonded force or energy interactions of the coiled and extended A2 tails with the B pentamers in each configuration modeled.

Differential toxicity between cholera toxin and *E. coli* heat-labile enterotoxin is influenced by residues in the A2 tail. We have conducted 350 ns of standard and steered molecular dynamics (SMD) simulations across many confirmations and configurations to observe interactions between the A2 tail and the B pentamer. SMD was initiated on the representative structures on the basis of clustered results and included two mutant conformations. Force profiles have been generated along a transition pathway to extend the A2 tail from ten 1.5 ns simulations for each of two configurations in CT and one in LT. The relative structural stabilities of the holotoxins were evaluated by computing nonbonded forces and energies between the A2 tail and B pentamer. We sought to understand how a limited number of amino acid changes between cholera and enterotoxin could significantly change the biophysical properties of their toxin complexes to modulate their efficacy while still maintaining overall complex integrity. We chose to characterize the macromolecular environments of both toxins using wild-type, tail-swapped, and individual F223D and G225D mutation models.

We hypothesize that the A2−B pentamer interactions affect toxin stability and toxicity and that CT has stronger interactions than the LT, enhancing its stability during retrograde transport and leading to increased toxicity. We seek to evaluate A2−B pentamer interactions to gain mechanistic insight into the differential toxicity between the CT and LT.

2. MATERIALS AND METHODS

2.1. Molecular Simulations. Molecular dynamics (MD) simulations were conducted with NAMD 2.6.[18] Initial coordinates were obtained from the WT CT structure (PDB id: 1XTC and 1S5E) and the WT LT structure (PDB id: 1LTS) (Table 2). Two addition models of the CT holotoxin were constructed with F223D and G225D mutations.

Unresolved coordinates were added on the basis of internal coordinates defined in the CHARMM22 force field.[19] Unresolved coordinates of side chain atoms were added with

Table 2. Initial Coordinates of the CT and LT Structures

PDB id	description	resolution (Å)
1XTC	WT CT holotoxin: helical A2[2]	2.4
1S5E	WT CT holotoxin: elongated A2[4]	1.9
1LTS	WT LT enterotoxin[6]	1.95

Table 3. Total of 350 ns of Simulation Divided into Trials and Total Duration of Subset

simulation set[a]	trials[b]	total duration (ns)
WT CT holotoxin with His$_{233}^{0}$	4 × 10	40
WT CT holotoxin His$_{233}^{+}$/MD	10 × 1	10
WT CT holotoxin His$_{233}^{0}$/SMD	10 × 1.5	15
WT CT holotoxin His$_{233}^{+}$/SMD	10 × 1.5	15
WT CT tailswap	3 × 10	30
CT holotoxin: F223D	4 × 5	20
CT holotoxin: G225D	4 × 5	20
WT CT extended with His$_{233}^{0}$	4 × 10	40
WT CT extended tailswap	4 × 10	40
CT extended: F223D	4 × 5	20
CT extended: G225D	4 × 5	20
WT LT/MD	5 × 10	50
LT tailswap helical A2/MD	5 × 3	15
LT tailswap helical A2/SMD	10 × 1.5	15

[a]Histidine 233 was evaluated in both a neutral and protonated configuration on the basis of the pK_a analysis from UHDB and a range of pH conditions in the cell. [b]The initial velocity was generated randomly on the basis of the Boltzmann distribution at 310 K.
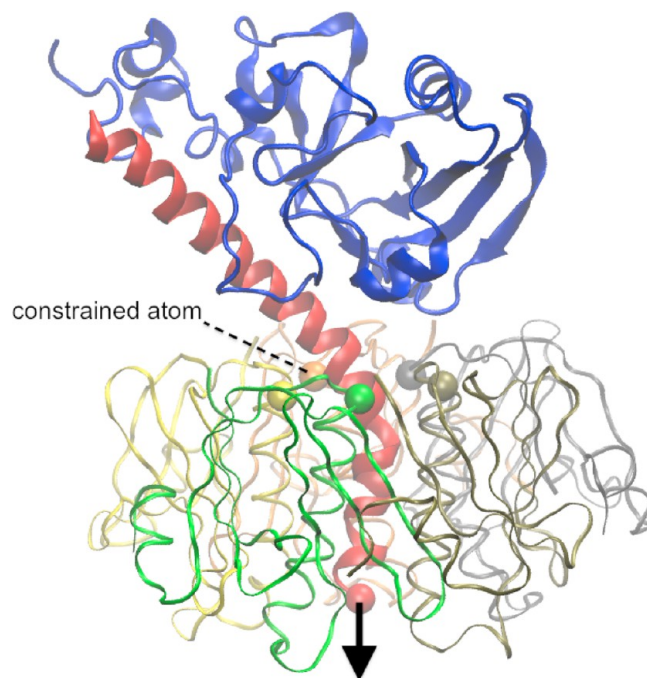

Figure 3. Application of constraints and restoring forces during steered molecular dynamics simulation: Five constrained atoms on the B pentamer are rendered as balls and colored by subunit. The arrow shows the force vector applied on the C-terminus of the A2 tail.

DeepViewer.[20] Hydrogen atoms were added to the modified structures with the HBUILD function of the CHARMM29 program.[21,22] The modified atoms were optimized with an energy tolerance of 0.001 kcal/mol using adopted basis Newton−Raphson (ABNR) minimization and a maximum

Table 4. SMD Constrained Atoms

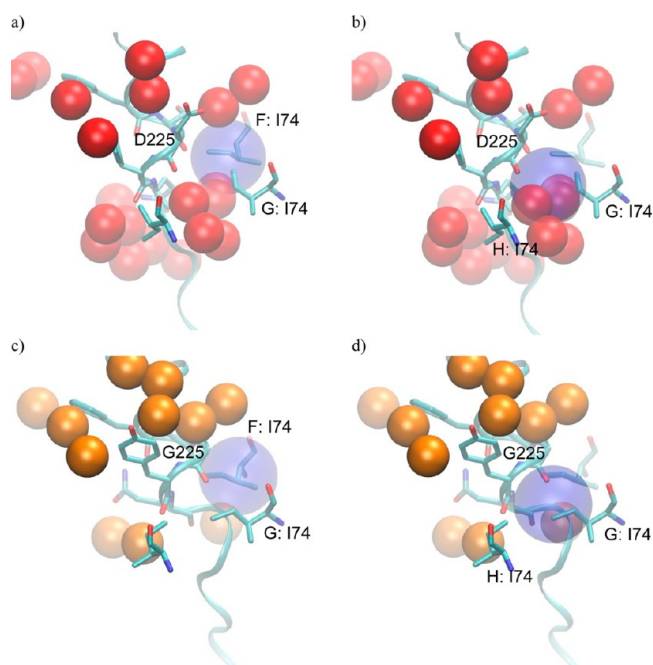| ID#	subunit	resid	atom	X	Y	Z
1	D	77	Cα	1.291	−5.081	4.261
2	E	77	Cα	2.971	3.708	−0.553
3	F	77	Cα	−1.777	2.109	−8.961
4	G	77	Cα	−4.918	−7.826	−8.037
5	H	77	Cα	−2.106	−11.592	0.570
6	C	240	Cα	−24.792	4.789	3.614

Figure 4. Sphere probes (light blue) with radius 2.8 Å used to access water occupancy: probes 1(a) and 2(b) for MD simulations of the WT LT; probes 1(c) and 2(d) for MD simulations of the WT CT. Location of either the G225 or D225 residue on the A2 tail in relation to isoleucine 74 on the F, G or H subdomain in the B pentamer.
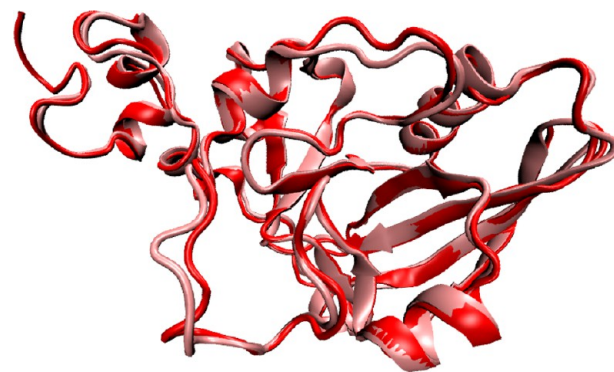

Figure 5. Structural alignment between LT and CT. Structural alignment of LTA (pink) and CTA (red) A1 subunit has a backbone RMSD of 0.84 Å (residues 5−170) demonstrates their close structural comparison.

iteration of 600. Solutions to the Poisson−Boltzmann equation using a finite-difference method were computed using the methods[23,24] implemented in the UHBD program[25] to predict the pK_a values for all ionizable residues in CT and LT. The structures were solvated, using VMD,[26] in a water (TIP3)[27] box with at least 13 Å of water between the surface of the protein and the edges of the box. The VMD default parameter of 2.4 Å
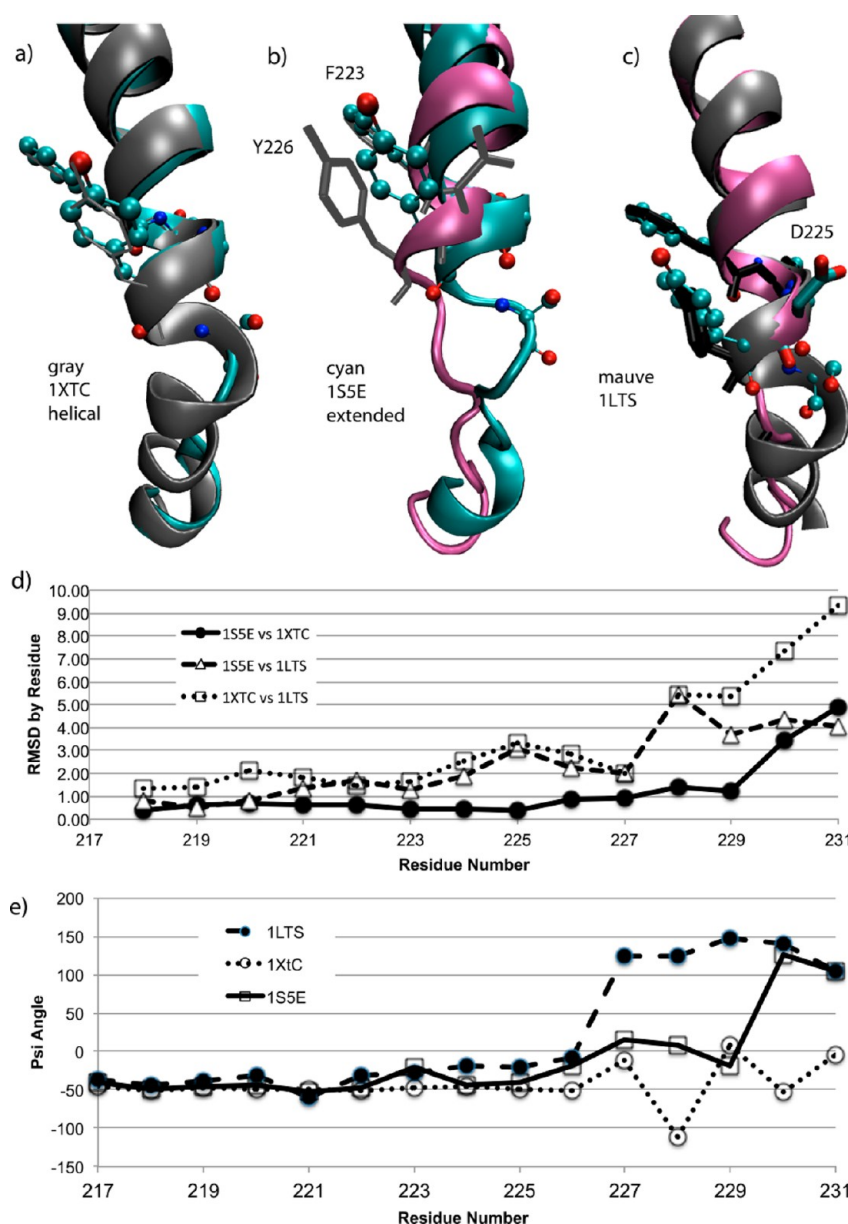
Figure 6. Comparison of all three tails identifying areas of common features between each of the pairs. The closest RMSD in the region from 217 to 228 is between 1S5E and 1XTC and is a region where all three structures initially have α helix. 1LTS departs first at 227. Further down the pore 1S5E and 1LTS share a more extended confirmation.

for the minimum distance between the water and the solute was used. An appropriate number of sodium or chloride ions was added to neutralize each system. Each system was minimized stepwise (200 steps of ABNR with fixed heavy atoms to minimize hydrogen atoms, 500 steps of ABNR with fixed backbone atoms of the protein to accommodate water and side chain atoms, 500 steps of ABNR with fixed C_α atoms, and 200 steps of steepest descent without constraints) using the CHARMM29 program. Afterward, each system was heated from 0 to 310 K with a 10 K/ps gradient and then equilibrated using NAMD with the CHARMM22 force field and evaluated against a convergence tolerance. Subsequently, multiple trials of the production run were conducted in 10 ns (ns) intervals and trajectory data points stored every 1 ps. Different initial velocities were assigned for each trial. The *NPT* ensemble with constant pressure of 1 atm and a constant temperature of 310 K using periodic boundary conditions was applied for all the simulations, and long-range

electrostatic interactions were calculated by the particle mesh Ewald method[28] using a 12 Å cutoff. Bonds involving hydrogen atoms were constrained via the SHAKE[29] algorithm, allowing for a time step of 2 fs. Simulation configurations are summarized in Table 3.

A second model of LT was also built using coordinate information from the CT A2 tail in the helical conformation. This was motivated to test transition barriers from a helical A2 to an elongated conformation in the LT B_5 pore versus the CT B_5 pore. The LT structure (PDB id: 1LTS) was aligned with the CT structure (PDB id: 1XTC) on the basis of the backbone atoms of the B pentamer. The A subunit of LT was then replaced by the A subunit of CT. All of the variant residues in the A subunit of CT were modified to the corresponding residues in LT using DeepViewer.[20] The LT model with helical A2 was energy minimized and solvated in a water box. Three 5 ns MD simulations of the LT model with different initial velocities
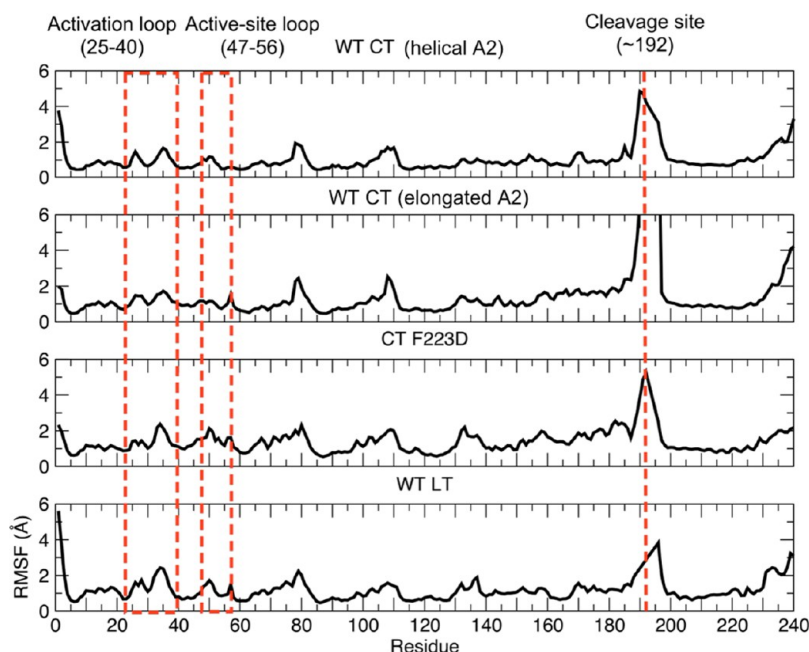
Figure 7. RMSF of backbone atoms throughout the MD simulations.

were conducted and the trajectories were combined. The MD data set was clustered on the basis of 26 dihedral angles on the backbone (ψ or φ) from Y226 to E239, i.e., the helix part in the B_5 pore. Three clusters were identified using a cutoff set to 50°. The 26 dihedral angles (features) of each frame were considered as one pattern. The Euclidean distance between each pattern and the cluster center was calculated using

$$\text{rms}(j,k) = \sqrt{\sum_{i=1}^{26} \left(\text{center}(j,i) - \text{pattern}(k,i)\right)^2} \qquad \text{(eq 3-1)}$$

where j is the number of clusters and k is the number of patterns. When the rms(j,k) was less than the cutoff, pattern k was grouped into the cluster j, and the center(j,i) was updated using

$$\text{center}(j,i) = \frac{(m-1)\cdot\text{center}(j,i) + \text{pattern}(k,i)}{m} \qquad \text{(eq 3-2)}$$

where m is the number of members in cluster j. The two steps were repeated until all patterns were input. The frame that represents the center of the most populated cluster defined the initial conformation for the steered molecular dynamics simulation.

2.2. Steered Molecular Dynamics. Steered molecular dynamics (SMD) simulations were used to generate trajectories that included transitions between the helical and elongated A2 conformations that are apparent in the crystal structures of cholera toxin (1XTC vs 1S5E). Furthermore, LT trajectories were performed to evaluate differential tendencies in A2−B_5 interaction energies. Inter- and Intra-residue forces and interaction energies were evaluated to access possible transition barriers in elongating the A2 tail and its KDEL sequence. The SMD simulations were configured on the basis of extensions to a standard MD protocol in NAMD. A set of constraint forces was applied symmetrically on the CT B pentamer as defined in Figure 3 and Table 4. These points were chosen to prevent any moment or translation motions of the holotoxin during the time course of the simulations. The perturbation forces along
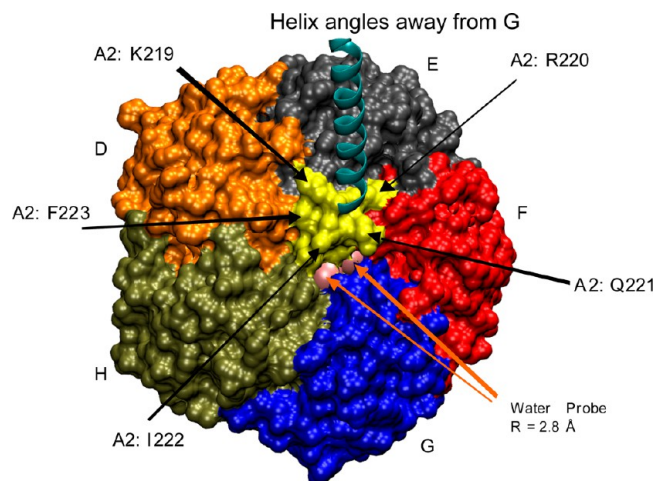

Figure 8. Top view of the B pentamer with selected residues from the A2 tail. The nomenclature follows the convention of O'Neal et al. (Supporting Information). The yellow cap is made up of residues K219 to F223 on the A2 tail. A gap at the A2 interface with B5 allows water to access other buried residues. Two pink spheres represent the water probes.

the helix center line, unit vector (0.885X, 0.311Y, 0.345Z), was computed on the basis of a force constant of 7.2 (kcal/mol)/Å² and a pulling velocity of 0.00004 Å/time step. Each constraint force was calculated by

$$F_{i(x,y,z)} = k\cdot(P_{o,i(x,y,x)} - P_{c,i(x,y,z)}) \qquad \text{(eq 3-3)}$$

where F_i is the force of the ith constraint, P_o is the initial position, and P_c is the constraint current position. And the restoring force was calculated by

$$F_x = k\cdot(P_{o,x} - u_x\cdot V\cdot t - P_{r,x})$$

$$F_y = k\cdot(P_{o,y} - u_y\cdot V\cdot t - P_{r,y})$$

$$F_z = k\cdot(P_{o,z} - u_z\cdot V\cdot t - P_{r,z}) \qquad \text{(eq 3-4)}$$
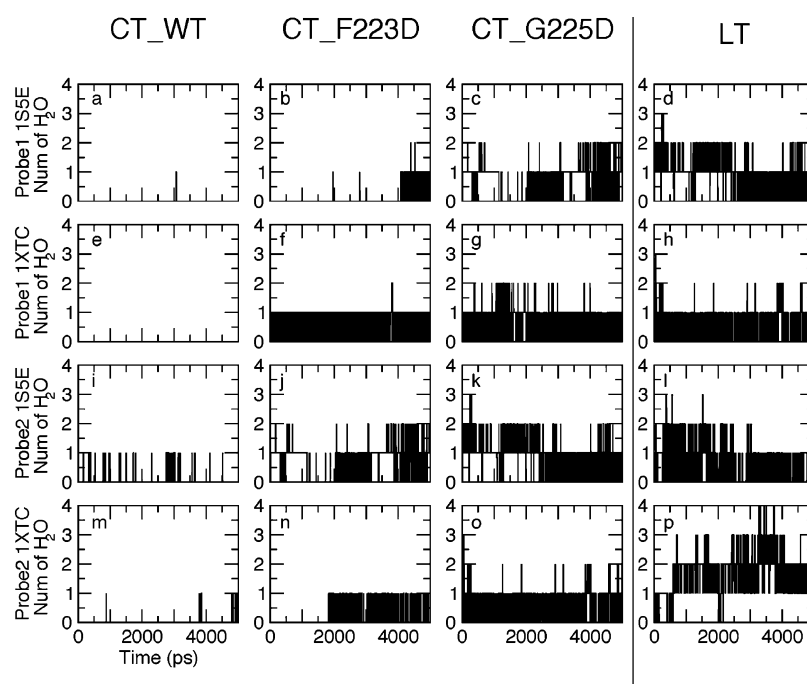
Figure 9. Summary of water occupancy as measured in MD simulations. Column 1: both the wild-type extended tail (1S5E) and the helical tail (1XTC) show a propensity to be more dry at probe 1 and probe 2. Column 2: the CT F223D mutant. Column 3: the CT G225D mutant mimics the water occupancy that in observed for LT in column 4.
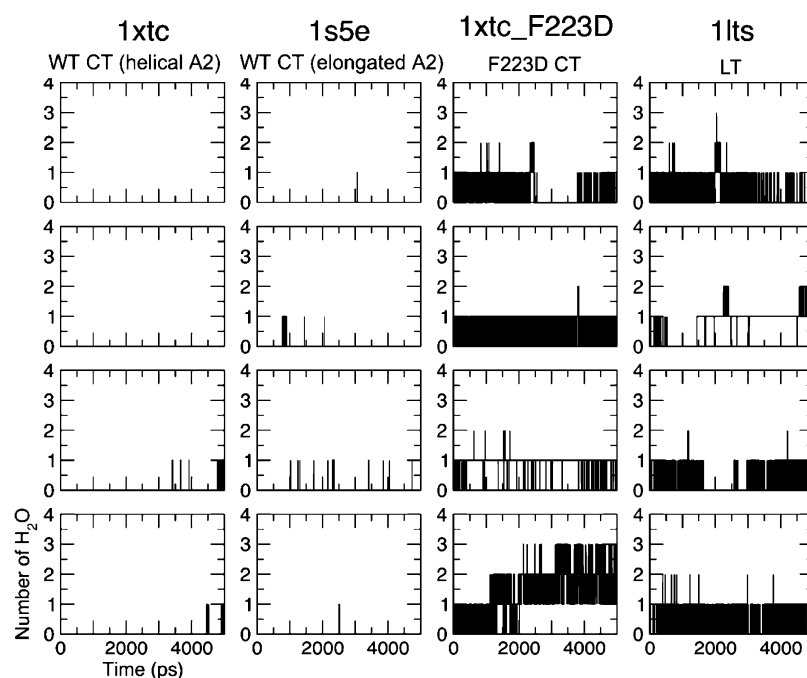

Figure 10. Water occupancy of probe 1 measured in multiple MD simulations. The number of water molecules monitored in the MD simulations at the location of probe 1. Column 1 is wild-type CT with helical A2, column 2 is wild-type CT with elongated A2, column 3 is the CT F223D mutant with helical A2 (for extended A2 see previous figure), and column 4 is LT.

where F is the restoring force, P_o is the initial position, P_r is the current position for the application of the restoring force, and V is the pulling velocity. The displacement, restoring forces, and restoring force application position were logged every 50 frames.

2.3. Water Probes. Two probes were defined to evaluate the water occupancy near the top of the central pore. The rationale to count the number of waters at the probe was guided

by trajectory visualizations in which it was apparent that each configuration has a different tendency to allow water to penetrate regions around G/D225 on the A2 tail near the initial intersection with the B pentamer. These probes were placed at the midpoint of the triangle defined by residues A2:G/D225, F:I74, and G:I74 for probe 1 and residues A2:G/D225, G:I74, and H:I74 for probe 2, respectively (Figure 4). The occupancy was treated as true for waters within 2.8 Å from that center.
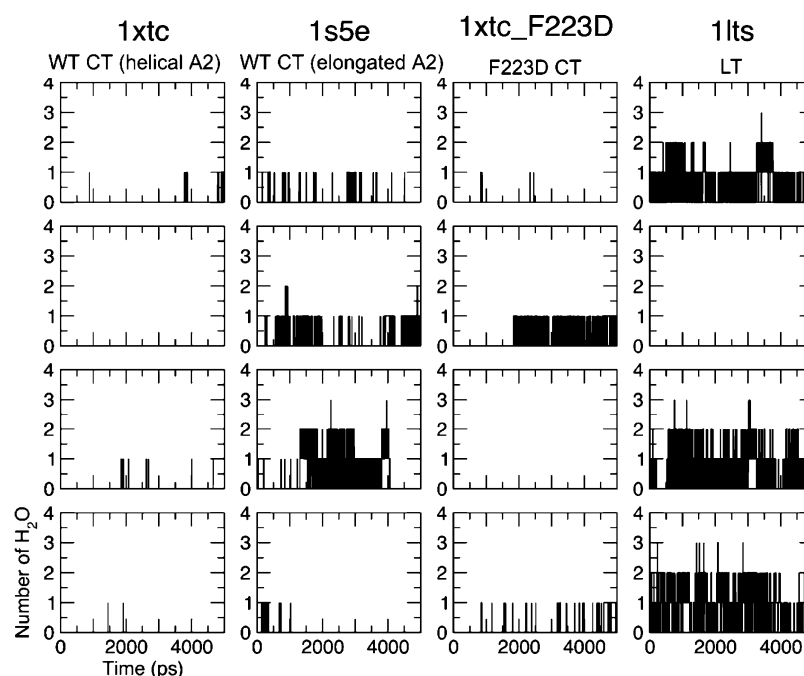
1053

dx.doi.org/10.1021/jp506509c | J. Phys. Chem. B 2015, 119, 1048−1061

Figure 11. Water occupancy of probe 2 measured in multiple MD simulations. The number of water molecules monitored in the MD simulations at the location of probe 2. Column 1 is wild-type CT with helical A2, column 2 is wild-type CT with elongated A2, column 3 is the CT F223D mutant with helical A2, and column 4 is LT.
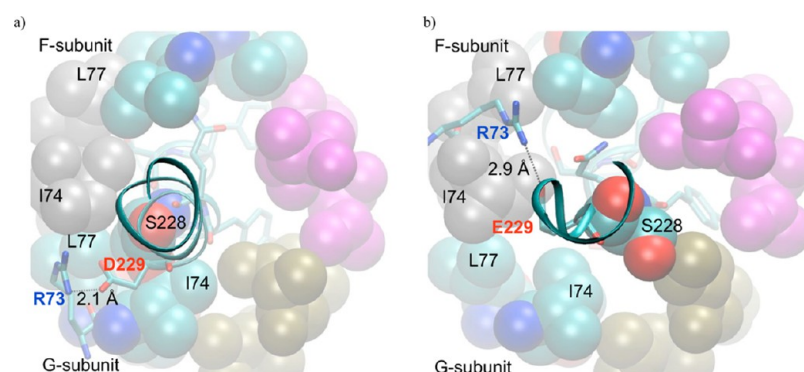

Figure 12. Comparison of CT and LT interactions that gate water access in the B_5 central pore. The bottom view of B_5 shows a salt bridge between A2:D229, and one of the B5:R73 residues mediates the accessibility of water by changing the relative displacement of the A2 tail in the B5 pore. (a) CT has a stable interaction with G:R73 opposite from the A2 bend, restricting water accessibility. (b) LT has a salt bridge with F:R73 allowing water passage.

2.4. Solvent Accessible Surface Area. The solvent accessible surface area (SASA) was computed using a Connolly radius of 1.4 Å.[30] Residues I74, L77, and T78 on the B pentamer were evaluated to assess the extent in which CT, LT, and the A2 tail-swapped mutants allowed solvent to disrupt the hydrophobic interactions between the A2 tail residues 223–227 and the B pentamer. A 10.0 Å cutoff was used during the computation.

2.5. Interaction Potential Forces and Pull Forces. The resultant force on each residue was computed from the interaction potentials of all atoms from other residues within 8 Å. The INTERACTION routine in the CHARMM29 program was used to gather the interaction potentials and force vectors on each atom.

The pull force was also recorded for SMD trajectories by the NAMD tclForcesScript. It was logged every 50 frames (0.1 ps) and a resultant extension magnitude and displacement X, Y, and Z components computed.

2.6. Conventions for Statistical Results. Calculations of both electrostatic and van der Waals energies were completed using an NAMD tcl script to evaluate A2 tail residue interactions with the B pentamer. Results were tabulated using the statistical package R, and statistical analysis was completed using the two-sample Z test to compare the significance of differences in means using a criterion of 0.05 for the P values.

3. RESULTS AND DISCUSSIONS

3.1. Alignments and MD Simulations. Crystal structures of CT and LT were aligned to explore the conformational difference. The structural alignment of the A1 domains shows a close conformational comparison with a backbone RMSD equal to 0.84 Å (Figure 5), further showing that the CT and LT sequence identity corresponded to structural similarity. The A2 tails were aligned between the CT structures with two forms of A2 (helical and elongated, PDB ids: 1XTC and 1S5E) in Figure 6.
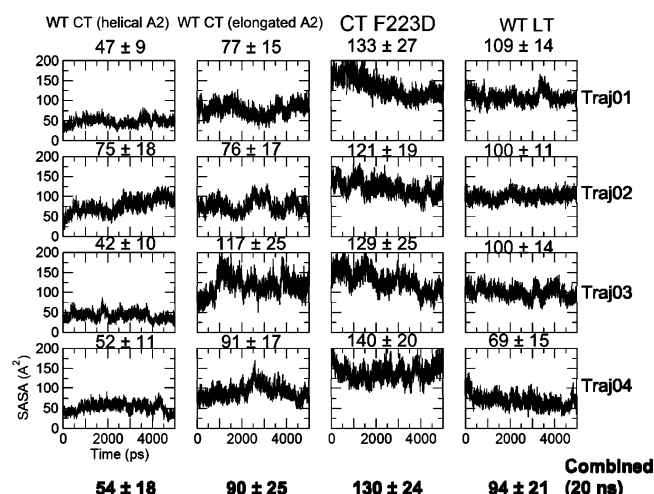
Figure 13. Solvent accessible surface area at the A2–B$_5$ interface. Solvent accessible surface area contributed by I74, L77, and T78 on the B pentamer with a probe radius of 1.4A.

The A2 tails were also aligned between the elongated CT (PDB id: 1S5E) and LT (PDB id: 1LTS) structures and the helical CT (PDB id: 1XTC) and LT (PDB id: 1LTS) structures. The RMSD's remain the closest between the two CT structures where the helical-like confirmation is maintained through residue D229. All three structures maintain a helix to Y226, but LT departs first where Q227 has backbone dihedrals in extended conformation of phi = −78 and psi = 124. The "elongated" CT structure still maintains close to helical confirmations with the "helical" CT variant until I230 when it also shifts to an extended conformation of phi = −57 and psi = 126 for two residues. The elongated CT A2 tail shifts back to a helix-like turn at residue T232 (phi/psi: −55/-49). Interestingly, both CT structures maintain similar conformations thoughout the bend of the A2 tail as it enters the B pentamer pore and past the gatekeeper of S228 in the region that we hypothesize is important for water occupancy and complex stability.

MD simulations each with different initial velocities were conducted to investigate the structural stability and A2–B$_5$ interactions in the multiple sets of holotoxin simulations. For each set, the trajectories were combined to form a large data set. RMSF analyses (Figure 7) were done with the combined data set to check the performance of backbone fluctuations by residue. The simulations exhibit similar patterns, having relatively larger fluctuations on the activation loop, active-site loop, cleavage site, and N- and C-termini. Though loops, cleavage sites, and termini are expected to be more flexible, we did not find that they had a correlation to A2-dependent holotoxin stability.

3.2. Water Occupancy in the B$_5$ Pore. The A2 helix makes a turn as it enters the B$_5$ pore. Five residues, K219–F223, ring the pore and cap the top of the pore. Our molecular dynamics simulations showed a gap opposite the bend of the A2 helix (Figure 8). This gap allows water molecules to access the top of the pore and disrupt interactions between the two subunits. Interestingly, the water occupancy of void spaces in the pore at position 1 and position 2 revealed that CT excluded water efficiently near the top of the pore as measured by the occupancy at probe 1, whereas LT did not (Figures 9 and 10: columns 1 and 2 vs column 4). These strong nonpolar interactions in CT were true for both helical and elongated A2 conformations in CT (Figures 9 and 10: column 1 vs 2). The relationship between water occupancy further collaborated experimental data by Tinker et al.[17] of weaker hydrophobic interactions in the F223D mutant. The simulations of the F223D mutant allowed solvation at probe 1 (Figure 10: column 3). The examination of water occupancy at the location of probe 2 (Figure 11) showed consistent results where the WT CT with helical A2 continued to exclude water. Alternatively, the LT allowed significant access in three of four simulation sets. Typical examples can be visualized in movies of water molecules near the top of the B pentamer pore (Supporting Information).

To further examine which atomic interactions distinguish the behavior of CT versus LT in their propensity to exclude water, a view from the bottom of the B pentamer was constructed for
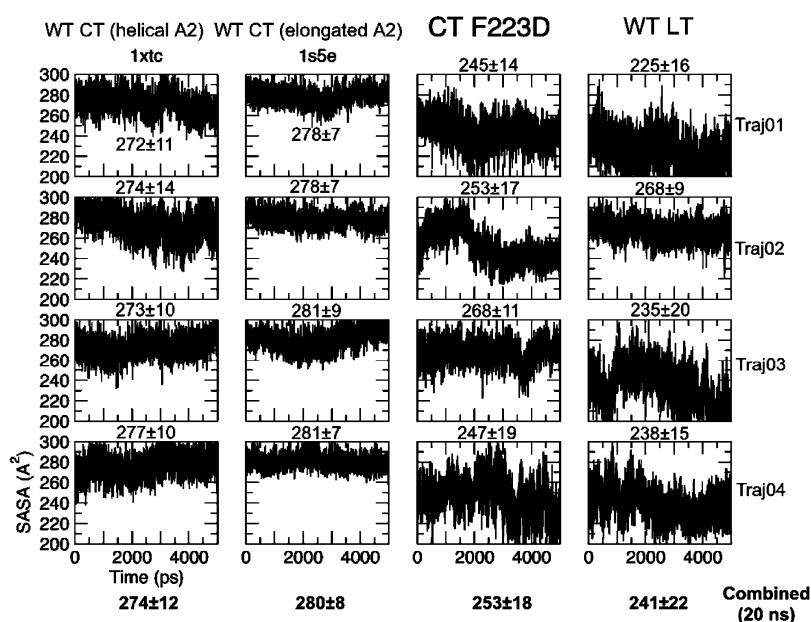

Figure 14. Contact surface between S228 and the B pentamer. Both wild-type helical (column 1) and extended (column 2) had higher contact areas than the F223D helical mutant (column 3) and the wild-type LT (column 4).
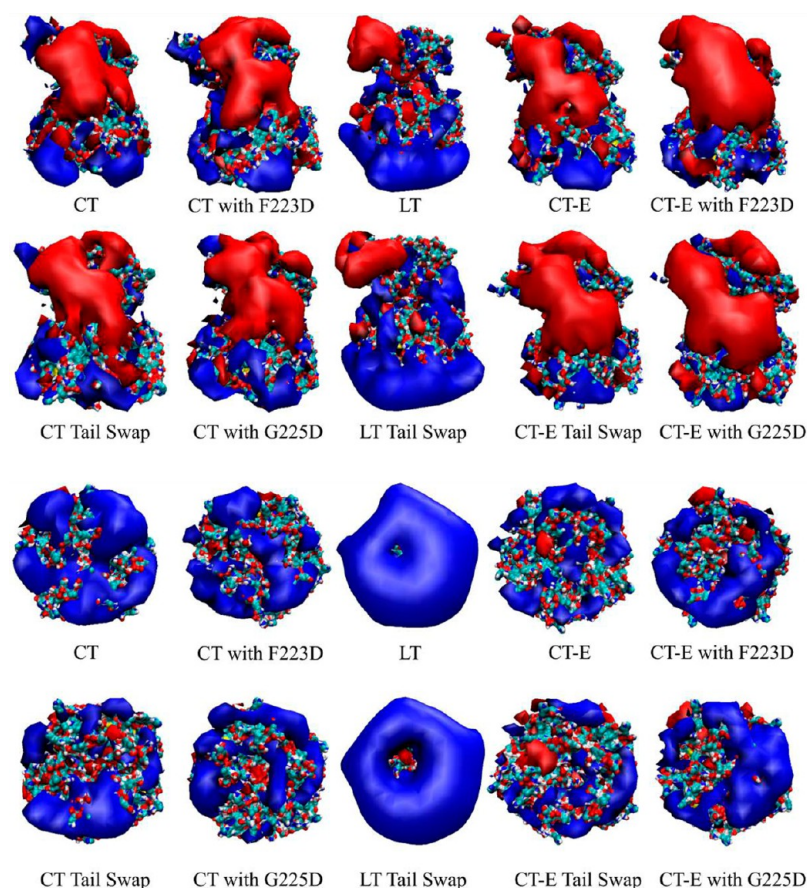
Figure 15. Electrostatic potential surfaces. Rows 1 and 2 are a front view. Rows 3 and 4 are a bottom view. Blue represents +1 and red, −1 ((kcal/mol)/e).

both toxins (Figure 12). The CT forms a salt bridge between A2:D229 and B_5:R73 on the G-subunit that moves S228 and the central α helix toward the pore edge and blocks water passage. The LT forms a salt bridge between E229 and the F-subunit R73, allowing water to move further up into the pore.

3.3. Solvent Accessible Surface Area. A comparison of the solvent accessible surface areas (SASA) contributed by I74, L77, and T78 on the B pentamer was computed with a probe radius of 1.4 Å and shows a dramatic increase in the CT:F223D mutant with an average of 130 ± 24 Å^2 versus only 54 ± 18 Å^2 in the WT CT with helical A2 (Figure 13). This indicates that the F223D mutant significantly disrupts the contact between A2 and B_5. Both the CT with elongated A2 and LT fell between these two extremes to values around 90 Å^2. Despite the trajectory of CT with elongated A2 having a larger SASA of 117 Å^2 in the third trial (Figure 13: column 2), and allowing initial water occupancy of probe 2 (Figure 11: column 2), water experienced limited passage through the pore and remained excluded from the site of probe 1. Interestingly, when the contact area between the S228 on the A2 tail and the surface of the B_5 pore is computed (Figure 14), it also correlates with the water occupancy data. Both the CT:F223D mutant (253 Å^2) and the LT (241 Å^2) have smaller contact areas because S228 acts as a gatekeeper that is open for the mutant or LT (i.e., not in close contact with the B_5 wall). In the wild-type CT the gate is closed and the corresponding contact area is larger (274 and 280 Å^2). The trajectories had surface contact with the gatekeeper, S228, higher for both the helical and extended CT trajectories, which is also consistent with our hypothesis.

3.4. Electrostatic Potentials. The electrostatic potentials were calculated in UHBD for each configuration, and a clear partition of differences in the electrostatic environment emerged between structures based on CT and structures based on LT. In Figure 15 are the resultant isosurface renderings for each toxin, where the blue represents +1 and the red, −1 ((kcal/mol)/e). The isosurfaces of LT are distinctly more positive than CT isosurfaces. There are a number of amino acid changes that contribute to the generally more positive isosurfaces in LT. Those amino acids, which are on the A subunit from cholera to enterotoxin, are D2G, Q18R, Q138R, S151R, D154N, G163R, and D209S. In addition, five histidines on the bottom edge of the B subunit of cholera are arginines in enterotoxin (H253R, H356R, H459R, H562R, and H665R). In CT and LT, the changes in electrostatic potential of the B pentamer is somewhat mitigated by the fact that the complex binds ganglioside (GM1) overpowering differences in surface charge.

3.5. Interpolation of the Isopotential on a Cylinder in the Pore. To further explore the biophysical environments that differentiate the CT and LT macromolecules and evaluate the differences in electrostatic potential in the core of the protein along the length of the A2 tail, we generated a cylinder mesh that was transformed into place and wrapped around the A2 tail (Figure 16). The heat map generation subroutine allowed for extraction of the cylinder from the toxin PDB and for 2D representation of the interpolation results (Figure 17).

There is a change in potential comparing the CT wild type to the LT tail swap. This is a result of the G225D mutation on the
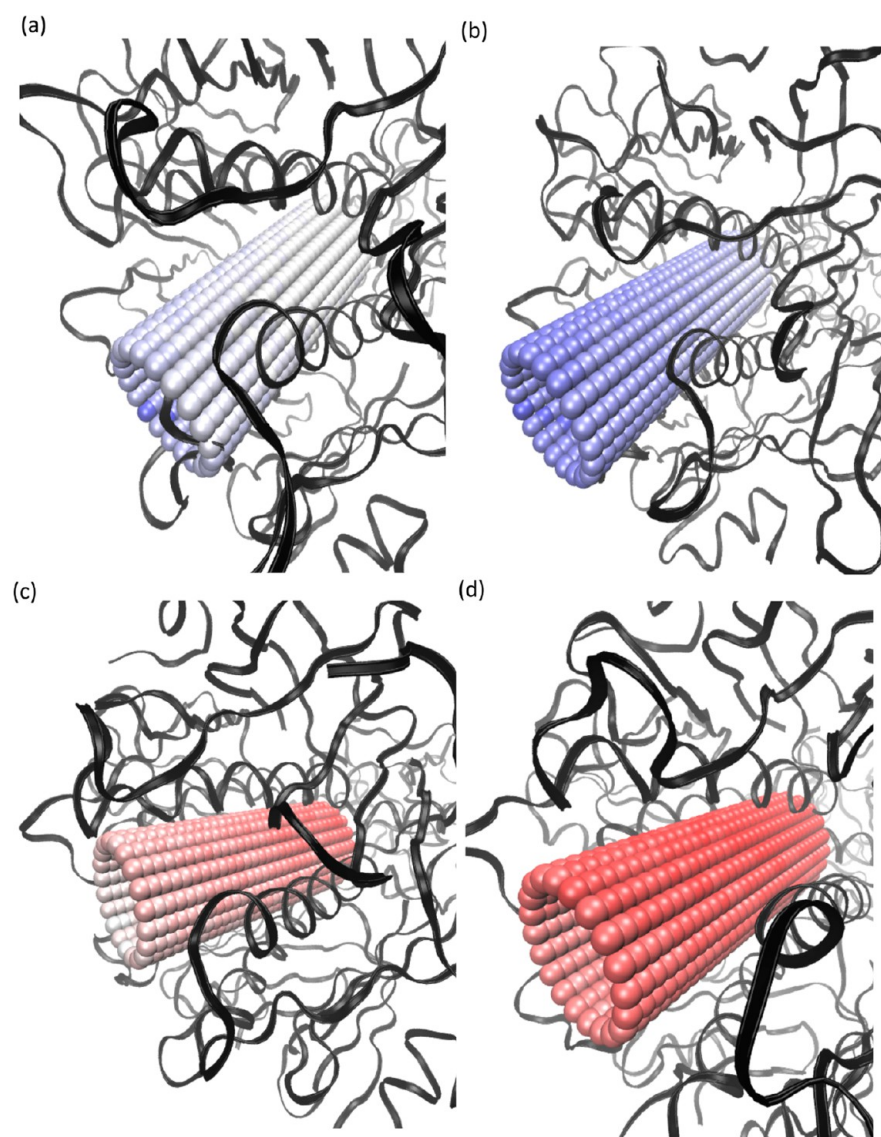
Figure 16. Postinterpolation representation. The interpolated potential value is stored on each mesh node and visualized on the cylinder still inserted inside the B-pore. Blue represents positive potential ((kcal/mol)/e), white represents neutral, and red represents negative. (a) LT wild-type model. (b) LT with CT tail-swap model. (c) CT wild-type model. (d) CT with LT tail-swap model.

A2 tail. This also explains why when the LT wild type is compared with the CT tail swap, the potential becomes more positive, as the D225G amino acid change removes the negative charge. Inside the "pore" area, which we define as within 5 Å of the A2 tail, there is a residue difference A342 K on chain D (and the respective 4 other points on chain E, F, G, and H) between the CT and the LT B pentamer, resulting in the potential being more positive inside the LT pore.

3.6. Interaction Energies. Due to the near identical topology and structure of CT and LT and the observation that both the wild-type and tail-swapped constructs assembled into viable complexes, we examined interaction energies between the A2 tails and the B pentamers to see if the coordination of amino acids between the two domains affected the interface. The electrostatic energy trended in an expected destabilizing direction when the CT tail swap was evaluated as compared to the wild type. In both the helical and the elongated tail the shift was −912.4 to −773.2 ($P = 0.112$) and −786.2 to −616.9 kcal/mol ($P = 0.0559$), respectively, and is consistent with our hypothesis

(Table 5 and Table 6). The larger P values reflect the aggregate effect of all the residues of A2 tail in the B pentamer pore and their attempt to accommodate the change in environment when swapped. However, the P values for statistical significant were borderline with values of 0.112 and 0.0559 when judged against a typical criterion of $P = 0.050$. When trajectories that included a single F223D or G225D variation were evaluated, consistent disruptions of the interface were observed. CT maintains its hydrophobic patch around the lip of the B pentamer more than configurations that have a LT tail swap. Furthermore, that trend continues and is significant when a single amino acid substitution of G225D is evaluated with a change from −912.4 to −719.4 kcal/mol ($P = 0.0273$). The individual contribution of the G225D substitution in the elongated tail caused a significant shift from −4.1 to 11.2 kcal/mol ($P = 1.2 \times 10^{-6}$). The F223D mutation also disrupted the interface contact area and destabilized the van der Waals energy with a P value of 0.00317 (F223D mutated full tail interaction) and 2.99×10^{-7} (F223D individual interaction). In CT to CT tail-swapped trajectories, the I230V amino acid change results
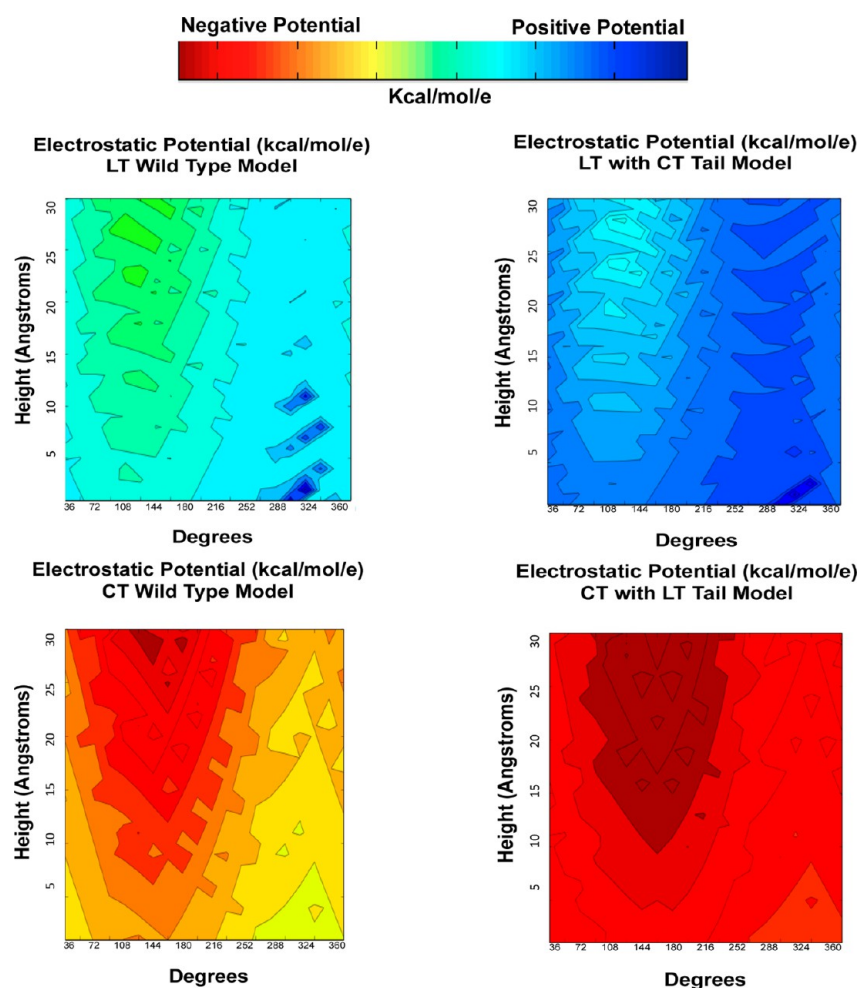
Figure 17. Heat map representation of interpolation results (2D rendering in Matlab).

in an destabilizing change in van der Waals energy due to a larger contact area of I230 with the B. The amino acid difference of H233Y, initially a surprise, results in a more favorable electrostatic energy. This is a byproduct of the seven ionizable residues on average throughout the trajectories that Y233 interacts within 5 Å on the B pentamer compared to only four with which H233 interacts.

3.7. Steered MD Simulations. Constant-velocity steered molecular dynamics (SMD) simulations were conducted to extend the helical A2 in the B_S pore of the CT and in the LT model. The resistance of the A2 helix and interactions between the A2 and B pentamer slowed down the extension of the A2 helix and the A2 helix was completely extended in 1.5 ns. The force was increased in the beginning due to the resistance and the average maximal force of the 10 runs is 23.8 ± 1.9 (kcal/mol)/Å. Another set of SMD simulations was conducted with a protonated H233 in CT to investigate the role of H233 during the extension of the A2 helix. The average maximal force (23.1 ± 1.6 (kcal/mol)/Å) does not show a significant difference from the results of CT with a neutral H233 (23.8 ± 1.9 (kcal/mol)/Å).

SMD simulations of LT were also conducted to investigate the propensity of the A2 helix extension in LT. The extension velocity of LT is slower than that of CT, and the average maximal force of the 10 runs reaches 29.6 ± 2.0 (kcal/mol)/Å to overcome the resistance of the A2 helix and the A2−B_S interactions in LT. The stability of the complex is most strongly

influenced by the A2/B pentamer interactions at the top of the pore from residues K219 through S228. Alternatively, the barriers of helix−coil transitions are more influenced by the interactions of the A2/B pentamer near the very end of the C-terminus, residues I230 through L240. Our experiments uncovered that the two phenomena are partly decoupled.

3.8. Differences in Hydrogen-Bonding. The distances between i to $i + 4$ residues along the A2 tail backbone of CT both with and without a protonated H233 side chain, and in a model of LT that was initialized in a helical A2 conformation, were monitored throughout the SMD trajectories. Interestingly, the interaction in CT between the H233 O atom and the K237 N backbone atom tended to break earlier (at 377 ± 60 ps) versus the stable distance in LT between Y233 O and the R237 N backbone atom (at 575 ± 118 ps). The characterization of CT versus LT was also differentiable in a strong hydrogen bond between the D231 O atom and the R235 N backbone atom in CT, whereas the same interaction was significantly weaker in LT. The CT interaction of I230 O with the N234 N backbone atom was marginal compared to that in LT. These observations were further correlated to energies between the A2 tail and the B pentamer decomposed by residue. Clearly, the sequence change from CT G225 to LT D225 would significantly change the charge contribution to the A2 interaction energy with B_S. Also the interaction energy of LT Y233 is much lower than the corresponding residue in CT, H233. This leads to a relatively strong hydrogen bond along the

Table 5. Statistical Analysis Nonbonded Interactions Energies (kcal/mol) of Trajectories in Helical CT Wild-Type (WT) and Tail-Swap (TS) Configurations Evaluating the A2 Tail to B Pentamer (1) or the Individual Residue (2)

Configuration	Mean	STD	P-value	Sig
CT WT Electrostatic[1]	-912.4	84.8		
CT TS Electrostatic[1]	-773.2	90.3	0.112	trend
CT F22D Electrostatic[1]	-946.6	97.5	0.708	
CT G225D Electrostatic[1]	-719.4	90.1	0.0273	*
CT WT van der Waals[1]	-116.0	8.7		
CT TS van der Waals[1]	-105.7	7.1	0.192	trend
CT F223D VDW[1]	-92.4	7.3	0.00317	*
CT G225D VDW[1]	-102.3	7.7	0.0955	trend
F223 Elect Contribution[2]	-5.7	1.5		
F223D Elect Contribution[2]	14.1	6.0	1.30E-07	*
G225 Elect Contribution[2]	-3.9	2.2		
G225D Elect Contribution[2]	-8.8	10.5	0.442	
F223 VDW Contribution[2]	-6.8	1.2		
F223D VDW Contribution[2]	-2.5	0.5	3.00E-07	*
G225 VDW Contribution[2]	-4.3	1.0		
G225D VDW Contribution[2]	-2.5	1.6	0.148	trend

Table 6. Statistical Analysis Nonbonded Interactions Energies (kcal/mol) of Trajectories in Extended CT Wild-Type (WT) and Tail-Swap (TS) Configurations Evaluating the A2 Tail to B Pentamer (1) or the Individual Residue (2)

Configuration	Mean	STD	P-value	Sig
CT WT Elect[1]	-786.2	95.0		
CT TS Elect[1]	-616.9	82.0	0.0559	*
CT WT VDW[1]	-108.9	7.4		
CT TS VDW[1]	-115.9	8.2	0.369	
G225 Elect Contribution[2]	-4.1	0.9		
G225D Elect Contribution[2]	11.2	5.4	1.20E-06	*
T232 Elect Contribution[2]	-17.9	5.7		
T232I Elect Contribution[2]	-4.8	2.0	0.00069	*
H233 Elect Contribution[2]	-9.5	4.8		
H233Y Elect Contribution[2]	-3.4	8.7	0.373	
G225 VDW Contribution[2]	-3.3	0.5		
G225D VDW Contribution[2]	-4.4	0.5	0.029	*
T232 VDW Contribution[2]	-5.4	2.0		
T232I VDW Contribution[2]	-9.7	1.1	0.00571	*
H223 VDW Contribution[2]	-7.6	1.4		
H233Y VDW Contribution[2]	-11.2	1.3	0.00777	*

backbone of LT, whereas in CT the side chain interactions of H233 to R67(B$_5$) overpower the i to $i + 4$ helix interactions and allow the secondary structure to relax earlier in the trajectories.

4. CONCLUSIONS

The differential toxicity of CT and LT may be influenced by a number of structural features associated with the A2 tail. Experimental data have shown the variance of the A2 sequence between CT and LT can affect the stability and toxicity of the holotoxins.[15,17] Additional experimental data have demonstrated that the hydrophobic patch between the A subunit and the B pentamer is important to complex stability.[17] The variant A2 sequence may also influence the helical and elongated forms of A2 in the B$_5$ pore and further impact the accessibility of the K/RDEL motif to enhance the efficiency of intoxication.

MD and SMD analyses are reported here with the holotoxin structures of CT and LT to assess the effects of the sequence variance on the hydrophobic interface and the equilibrium of the helical versus elongated A2 tail. We have evaluated interaction energies, forces, and solvent accessible surface areas in the interface between the C-terminal A2 tail of the catalytic domain and the pore in the B pentamer. The cholera holotoxin has a higher propensity to exclude water and has a reduced SASA in the top of the central pore of the B pentamer around I74, L77, and T78. This observation was apparent in water occupancy data collected at two probe locations and also apparent in the increased solvent accessible surface area (SASA); the SASA of CT is 54 Å^2 and that of LT is 94 Å^2. A significant difference between CT and LT was the observation that S228 maintained more (helical, 274 Å$^{2;}$; elongated, 280 Å^2) contact area than LT (241 Å^2), which is

indicative of the role that S228 plays as a gatekeeper, limiting the diffusion of water at the top of the CT pore.

Our analysis of the CT tail-swap configuration demonstrated that the interaction energies between the A2 tail and the B pentamer trended toward destabilization for both the electrostatic contribtion and the van der Waals contribution, which is consistent with experimental data. Even more significant (P value of 0.0273) was the destabilization due to a substitution G225D. Though the F223D mutation is not observed in the sequence difference between CT and LT, we choose to also evaluate it to complement the experimental data by Rodighiero et al.[15] and we found that the disruption in the hydrophobic interface between the A2 tail and the B pentamer significanly reduced the van der Waals contribution to the interaction energy (P value 0.00317).

Interestingly, seven residues on the A subunit of LT are changed from either negative charges to neutral or from neutral to positive, thus increasing the positive electrostatic enviornment of the macromolecule. In addition, five histidines on the base of the B pentamer are also changed to arginines in LT, increasing the positive electrostatic environment on the membrane binding face of the complex. These changes result in a significant difference in the overall electrostatic potentials and can be easily visualized in the isopotential surface maps presented here; however, they do not appear to be a dominant affect in the interface stability as measured by the interaction energies.

SMD simulation results show that the extension of the A2 helix in LT needs larger forces than the extension in CT. This implies that the energy barrier between the helical and

elongated A2 in CT is lower than the barrier in LT. The force and energy profiles as decomposed into each residue were used to identify their roles contributing to the interactions in the A2−B$_5$ interface. Specifically, H/Y233 shows a difference in the interaction energies at the A2−B$_5$ interface and also shows that the H233O−K237N hydrogen bond of CT breaks earlier due to the side chain−side chain interactions (H233Nδ1−B$_5$:R73Nη2 and H233Nε2−B$_5$:R67Nη2) overcoming the hydrogen bonds along the *i* to *i* + 4 helical axis. In our LT simulations the Y233 forms a hydrogen bond with B$_5$:E65 but has fewer interactions between it and the B$_5$ pore as compared to CT.

The extension of the helical A2 is forced by the SMD protocol, and we observed that H/Y233 and G/D225 had significant differences in the interaction energies between CT and LT. This is due to the two salt bridges formed by D225 in LT with R146 and R148.

Overall, our MD and SMD simulations demonstrate an A2−B$_5$ contact area in wild-type CT that can exclude water more efficiently than LT. The hydrophobic region would likely facilitate the stability of the AB$_5$ holotoxin and may underlie one of the causes for the increased toxicity of cholera toxin. Amino acid differences in the A2 tail between CT and LT influence destabilizing interactions in LT, contributing to the differential toxicity of cholera.

■ ASSOCIATED CONTENT

Ⓢ Supporting Information

A table of nomenclature used by the authors of key referenced crystal structures is included in the Supporting Information to clarify our use of chain names. Also, included are two movies that show the water occupancy of the elongated CT wild type (1S5E) and the LT wild type (1LTS) from typical molecular dynamics simulations showing that in LT more water passes through the top of the B pentamer. This material is available free of charge via the Internet at http://pubs.acs.org.

■ AUTHOR INFORMATION

Corresponding Author

*J. M. Briggs. E-mail: jbriggs@uh.edu.

Present Address

‡Washington University School of Medicine, 660 S. Euclid Ave. St. Louis, MO 63110.

Author Contributions

†These authors contributed equally

Notes

The authors declare no competing financial interest.

■ REFERENCES

(1) Lospalluto, J. J.; Finkelstein, R. A. Chemical and Physical Properties of Cholera Exo-Enterotoxin (Choleragen) and Its Spontaneously Formed Toxoid (Choleragenoid). *Biochim. Biophys. Acta* **1972**, *257*, 158−166.

(2) Zhang, R. G.; Scott, D. L.; Westbrook, M. L.; Nance, S.; Spangler, B. D.; Shipley, G. G.; Westbrook, E. M. The Three-Dimensional Crystal Structure of Cholera Toxin. *J. Mol. Biol.* **1995**, *251*, 563−573.

(3) Jobling, M. G.; Holmes, R. K. Identification of Motifs in Cholera Toxin A1 Polypeptide That Are Required for Its Interaction with Human Adp-Ribosylation Factor 6 in a Bacterial Two-Hybrid System. *Proc. Natl. Acad. Sci. U. S. A.* **2000**, *97*, 14662−14667.

(4) O'Neal, C. J.; Amaya, E. I.; Jobling, M. G.; Holmes, R. K.; Hol, W. G. Crystal Structures of an Intrinsically Active Cholera Toxin Mutant Yield Insight into the Toxin Activation Mechanism. *Biochemistry* **2004**, *43*, 3772−3782.

(5) Sears, C. L.; Kaper, J. B. Enteric Bacterial Toxins: Mechanisms of Action and Linkage to Intestinal Secretion. *Microbiol. Rev.* **1996**, *60*, 167−215.

(6) Sixma, T. K.; Kalk, K. H.; van Zanten, B. A.; Dauter, Z.; Kingma, J.; Witholt, B.; Hol, W. G. Refined Structure of Escherichia Coli Heat-Labile Enterotoxin, a Close Relative of Cholera Toxin. *J. Mol. Biol.* **1993**, *230*, 890−918.

(7) Lencer, W. I. Microbes and Microbial Toxins: Paradigms for Microbial-Mucosal Toxins. V. Cholera: Invasion of the Intestinal Epithelial Barrier by a Stably Folded Protein Toxin. *Am. J. Physiol. Gastrointest. Liver. Physiol.* **2001**, *280*, G781−786.

(8) Teter, K. Toxin Instability and Its Role in Toxin Translocation from the Endoplasmic Reticulum to the Cytosol. *Biomolecules* **2013**, *3*, 997−1029.

(9) Wernick, N. L. B.; Chinnapen, D. J.-F.; Cho, J. A.; Lencer, W. I. Cholera Toxin: An Intracellular Journey into the Cytosol by Way of the Endoplasmic Reticulum. *Toxins* **2010**, *2*, 310−325.

(10) Lencer, W. I.; Constable, C.; Moe, S.; Rufo, P. A.; Wolf, A.; Jobling, M. G.; Ruston, S. P.; Madara, J. L.; Holmes, R. K.; Hirst, T. R. Proteolytic Activation of Cholera Toxin and Escherichia Coli Labile Toxin by Entry into Host Epithelial Cells. Signal Transduction by a Protease-Resistant Toxin Variant. *J. Biol. Chem.* **1997**, *272*, 15562−15568.

(11) Lencer, W. I.; Tsai, B. The Intracellular Voyage of Cholera Toxin: Going Retro. *Trends Biochem. Sci.* **2003**, *28*, 639−645.

(12) Tsai, B.; Rodighiero, C.; Lencer, W. I.; Rapoport, T. A. Protein Disulfide Isomerase Acts as a Redox-Dependent Chaperone to Unfold Cholera Toxin. *Cell* **2001**, *104*, 937−948.

(13) Tsai, B.; Rapoport, T. A. Unfolded Cholera Toxin Is Transferred to the Er Membrane and Released from Protein Disulfide Isomerase Upon Oxidation by Ero1. *J. Cell. Biol.* **2002**, *159*, 207−216.

(14) Schmitz, A.; Herrgen, H.; Winkeler, A.; Herzog, V. Cholera Toxin Is Exported from Microsomes by the Sec61p Complex. *J. Cell. Biol.* **2000**, *148*, 1203−1212.

(15) Rodighiero, C.; Aman, A. T.; Kenny, M. J.; Moss, J.; Lencer, W. I.; Hirst, T. R. Structural Basis for the Differential Toxicity of Cholera Toxin and Escherichia Coli Heat-Labile Enterotoxin. Construction of Hybrid Toxins Identifies the A2-Domain as the Determinant of Differential Toxicity. *J. Biol. Chem.* **1999**, *274*, 3962−3969.

(16) Ampapathi, R. S.; Creath, A. L.; Lou, D. I.; Craft, J. W.; Blanke, S. R.; Legge, G. B. Order-Disorder-Order Transitions Mediate the Activation of Cholera Toxin. *J. Mol. Biol.* **2008**, *377*, 748−760.

(17) Tinker, J. K.; Erbe, J. L.; Hol, W. G.; Holmes, R. K. Cholera Holotoxin Assembly Requires a Hydrophobic Domain at the a-B5 Interface: Mutational Analysis and Development of an in Vitro Assembly System. *Infect. Immun.* **2003**, *71*, 4093−4101.

(18) Phillips, J. C.; Braun, R.; Wang, W.; Gumbart, J.; Tajkhorshid, E.; Villa, E.; Chipot, C.; Skeel, R. D.; Kale, L.; Schulten, K. Scalable Molecular Dynamics with NAMD. *J. Comput. Chem.* **2005**, *26*, 1781−1802.

(19) MacKerell, A. D.; Bashford, D.; Bellott; Dunbrack, R. L.; Evanseck, J. D.; Field, M. J.; Fischer, S.; Gao, J.; Guo, H.; Ha, S.; et al. All-Atom Empirical Potential for Molecular Modeling and Dynamics Studies of Proteins Using the CHARMM22 Force Field. *J. Phys. Chem. B* **1998**, *102*, 3586−3616.

(20) Guex, N.; Peitsch, M. C. Swiss-Model and the Swiss-Pdbviewer: An Environment for Comparative Protein Modeling. *Electrophoresis* **1997**, *18*, 2714−2723.

(21) Brooks, B.; Bruccoleri, R.; Olafson, B.; States, D.; Swaminathan, S.; Karplus, M. CHARMM: A Program for Macromolecular Energy, Minimization, and Dynamics Calculations. *J. Comput. Chem.* **1983**, *4*, 187−217.

(22) Brooks, B. R.; Brooks, C. L., 3rd; Mackerell, A. D., Jr.; Nilsson, L.; Petrella, R. J.; Roux, B.; Won, Y.; Archontis, G.; Bartels, C.; Boresch, S.; et al. CHARMM: The Biomolecular Simulation Program. *J. Comput. Chem.* **2009**, *30*, 1545−1614.

(23) Antosiewicz, J.; McCammon, J. A.; Gilson, M. K. Prediction of Ph-Dependent Properties of Proteins. *J. Mol. Biol.* **1994**, *238*, 415−436.

(24) Antosiewicz, J.; Briggs, J. M.; Elcock, A. H.; Gilson, M. K.; McCammon, J. A. Computing Ionization States of Proteins with a Detailed Charge Model. *J. Comput. Chem.* **1996**, *17*, 1633−1644.

(25) Madura, J. D.; Briggs, J. M.; Wade, R. C.; Davis, M. E.; Luty, B. A.; Ilin, A.; Antosiewicz, J.; Gilson, M. K.; Bagheri, B.; Scott, L. R.; et al. Electrostatics and Diffusion of Molecules in Solution: Simulations with the University of Houston Brownian Dynamics Program. *Comput. Phys. Commun.* **1995**, *91*, 57−95.

(26) Humphrey, W.; Dalke, A.; Schulten, K. VMD: Visual Molecular Dynamics. *J. Mol. Graph.* **1996**, *14*, 33−38 27−38..

(27) Jorgensen, W. L.; Chandrasekhar, J.; Madura, J. D.; Impey, R. W.; Klein, M. L. Comparison of Simple Potential Functions for Simulating Liquid Water. *J. Chem. Phys.* **1983**, *79*, 926−935.

(28) Essmann, U.; Perera, L.; Berkowitz, M.; Darden, T.; Lee, H.; Pedersen, L. A Smooth Particle Mesh Ewald Method. *J. Chem. Phys.* **1995**, *103*, 8577−8593.

(29) Ryckaert, J.-P.; Ciccotti, G.; Berendsen, H. J. C. Numerical Integration of the Cartesian Equations of Motion of a System with Constraints: Molecular Dynamics of N-Alkanes. *J. Comput. Phys.* **1977**, *23*, 327−341.

(30) Connolly, M. Analytical Molecular Surface Calculation. *J. Appl. Crystallogr.* **1983**, *16*, 548−558.

1061

dx.doi.org/10.1021/jp506509c | *J. Phys. Chem. B* 2015, 119, 1048−1061